RSC Advances

PAPER

Cite this: *RSC Adv.*, 2016, **6**, 83126

Graphite–silicon alloy composite anodes employing cross-linked poly(vinyl alcohol) binders for high-energy density lithium-ion batteries

Seung-Hyun Yook,[a] Sang-Hyung Kim,[a] Cheol-Ho Park[b] and Dong-Won Kim*[a]

Received 18th June 2016
Accepted 22nd August 2016

DOI: 10.1039/c6ra15839k

www.rsc.org/advances

A new silicon alloy material composed of silicon nanoparticles embedded in Al–Fe–Ti–Ni matrix phases was synthesized and characterized. Using this alloy material, graphite–silicon alloy composite electrodes were prepared and investigated as anodes for lithium-ion batteries. Poly(vinyl alcohol)s (PVAs) with different degrees of cross-linking were used as polymer binders in these composite anodes. A systematic study demonstrated that the cross-linking of PVA with an appropriate amount of fumaric acid made the electrodes mechanically strong and remarkably improved the electrochemical performance of the composite electrodes. Their superior cycling performance could be attributed to strong adhesion of the three-dimensional PVA networks, which maintained good electrical contacts between the active materials, electronic conductors and current collectors during cycling. The graphite–silicon alloy composite electrodes exhibiting high capacities and good cycling stability showed promise as anodes for high-energy density lithium-ion batteries.

Introduction

An increasing demand for high-performance rechargeable batteries for various applications including portable electronic devices, electric vehicles and energy storage systems requires large improvements in the energy densities of the current lithium-ion batteries.[1–3] Graphite has been widely used as an active anode material in commercial lithium-ion batteries due to its low cost and long cycle life. However, the available capacity of graphite is limited to around 350 mA h g^{-1}, which is close to its theoretical capacity of 372 mA h g^{-1}. In order to improve the energy density of lithium-ion batteries, silicon materials have been actively studied as attractive anode materials due to their high theoretical capacities, low reduction potentials and low cost.[4] However, silicon materials suffer from substantial volume changes during lithiation and delithiation, which are detrimental to the cycling stability of lithium-ion batteries. The mechanical stresses caused by repeated volume changes can fracture the silicon-based electrode, resulting in poor electrical contacts between the active materials, electronic conductors and current collector. As a result, a large capacity decline occurs during the repeated cycling. To solve these problems, many studies have been performed to investigate (1) the use of nanostructured silicon materials to mitigate volumetric changes,[5–7] (2) the use of silicon alloys with inert matrix phases comprising inert metals that do not react with Li^+,[8–11] (3) the use of composite electrodes consisting of graphite and silicon,[12–17] and (4) the use of functional binders to allow the electrode to adhere to the current collector and improve the coherence of active silicon particles.[18–25] However, to the best of our knowledge, there have been no studies combing the above approaches in order to obtain the silicon-based anodes with high capacity and good cycling stability for practical use in high-performance lithium-ion battery applications. In this study, we attempted to combine the latter three approaches (2, 3, and 4) to achieve high capacity while maintaining good cycling stability of the anode.

With regard to high-capacity silicon-based active material, we synthesized new silicon alloy that was composed of silicon nanoparticles embedded in Al–Fe–Ti–Ni matrix phases. Iron, titanium and nickel elements were selected as the inactive matrix to reduce the stress generated during cycling when active silicon particles undergo lithiation and delithiation.[9,26,27] Aluminum was also used due to its high electrical conductivity and lower cost than Ni and Ti.[10] Consequently, the matrix phases have a mechanical property to endure the stress generated by the volume expansion of Si during cycling in addition to high electrical conductivity for fast electron transfer to silicon. The as-synthesized silicon alloy particles were mixed with graphite powder showing good capacity retention to prepare the composite electrodes with high capacity and good cycling stability. In these composite anodes, poly(vinyl alcohol) (PVA)s with different degrees of cross-linking were employed as polymer binders to further improve the cycling performance. The effect of the degree of cross-linking on the interfacial adhesion

[a]*Department of Chemical Engineering, Hanyang University, Seoul 133-791, Republic of Korea. E-mail: dongwonkim@hanyang.ac.kr*

[b]*Next-G Institute of Technology, Iljin Electric Co. Ltd, Gyeonggi-do 425-100, Republic of Korea*

and cycling performance of the composite electrodes was investigated to identify the optimum binder composition.

Experimental

Synthesis of silicon alloy materials

Silicon alloy materials were synthesized *via* arc melting, followed by single-roll solidification methods (SRSM). Si (70 at%), Al (15 at%), Fe (5 at%), Ti (5 at%), and Ni (5 at%) metals were used as precursors to synthesize the silicon alloy. Alloy buttons were obtained by arc melting in a Cu hearth using a non-consumable tungsten electrode in an argon atmosphere. The buttons were re-melted and solidified three times to ensure homogeneity. SRSM ribbons were produced by a graphite nozzle single-roll method in an inert atmosphere to prevent oxidation. Finally, silicon alloy particles were obtained by mechanically crushing the ribbons with zirconia beads in an attrition mill at 150 rpm.

Electrode preparation and cell assembly

PVA (M_w = 89 000–98 000) was purchased from Sigma Aldrich. Graphite powder (Btr New Energy Materials) and the as-synthesized silicon alloy particles were mixed at a mass ratio of 90 : 10, and the mixture was used as the active material when preparing the composite anode. The electrode slurry was prepared by mixing 92 wt% active materials (graphite and Si alloy) with 2 wt% Ketjen black and 6 wt% PVA binder in dimethyl sulfoxide (DMSO) solvent. Fumaric acid (Tokyo Chemical Industry), the cross-linking agent, was added at various concentrations (0, 2.5, 5.0, 7.5, and 10.0 mol% with respect to the PVA hydroxyl groups) into the slurry. The composite electrodes were prepared by coating the viscous slurry onto copper foil using a doctor blade. The electrodes were dried in a vacuum oven at 80 °C for 1 h and were further thermally treated at 150 °C for 6 h to induce esterification between PVA and fumaric acid. The active mass loading in the electrodes was about 3.4 mg cm^{-2} based on the total mass of graphite and Si alloy, corresponding to a capacity of approximately 1.6 mA h cm^{-2}. The composite electrodes will be designated as PVA-*x*, where *x* denotes the mol% of fumaric acid used to prepare the electrodes. The electrodes employing only graphite or silicon alloy were also prepared as control samples. In order to evaluate the cycling characteristics of the composite electrodes, a CR2032-type coin cell was assembled by sandwiching a polyethylene separator (ND420, thickness: 20 μm, Asahi Kasei E-materials) between the lithium electrode and the composite electrode. The lithium electrode consisted of a 100 μm-thick lithium foil (Honjo Metal Co. Ltd.) pressed onto a copper current collector. The cell was then injected with an electrolyte solution consisting of 1.15 M $LiPF_6$ in ethylene carbonate (EC)/ethylmethyl carbonate (EMC)/diethyl carbonate (DEC) (3/5/2 by volume) containing 5 wt% fluoroethylene carbonate (FEC) (battery grade, PANAX ETEC Co. Ltd.). All cells were assembled in a dry box filled with argon gas.

Characterization and measurements

The morphologies of the silicon alloy powders were examined using field emission scanning electron microscopy (FE-SEM, JEOL JSM-7600F) equipped with energy dispersive X-ray spectroscopy (EDS). In order to investigate the cross-sectional morphologies of the silicon alloy materials and composite electrodes, samples were cut using an argon-ion beam polisher (JEOL, IB-09010CP) at constant power in an inert Ar atmosphere to avoid chemical damage. Samples were transferred to the SEM chamber without any air exposure, and cross-sectional SEM images were obtained. X-ray diffraction (XRD) pattern of the silicon alloy powders was recorded on a Rigaku DMAX/2500 using Cu Kα radiation. Fourier transform infrared (FT-IR) spectra of the cross-linked PVA films were obtained with a JASCO FTIR-460 Plus spectrometer. For the electrode peel test, 3M tape was attached to the composite electrode. The taped electrode was weakly roll-pressed in order to ensure uniform attachment. The adhesive strength was then measured during detachment of the 3M tape.[28,29] Charge and discharge cycling tests of the composite electrodes were carried out at a current density of 0.8 mA cm^{-2} (0.5C rate) over a voltage range of 0.01 to 1.5 V using battery testing equipment (WBCS 3000, WonA Tech Co., Ltd.), unless otherwise specified. In the composite electrodes, C rate was calculated using the reversible capacity of the composite electrode (474.2 mA h g^{-1}) that was calculated using the capacities of graphite and silicon alloy multiplied by their corresponding weight fractions. Hereafter we refer to lithiation as the charge and delithiation as the discharge, based on the practical applications of lithium-ion batteries. The specific capacities were calculated based on the total mass of active materials (graphite and silicon alloy) in the composite electrode.

Results and discussion

Silicon alloy particles were obtained by mechanically crushing the ribbon-type alloy material. An SEM image of the silicon alloy particles is shown in Fig. 1(a), with particle sizes ranging from 0.5 to 2.0 μm. Cross-section polishing (CP)-SEM was performed with an argon-ion beam polisher to observe the cross-sectional microstructure of the silicon alloy material. As seen in Fig. 1(b), the alloy was composed of two different phases. According to the EDS analysis presented in Fig. 2, dark regions corresponded to silicon crystallites, while the light parts corresponded to inert metal phases composed of aluminum, iron, titanium and nickel, as previously reported for other silicon alloy materials.[10] Here, inactive metal phases help reduce the volumetric expansion of silicon and enhance the electronic conductivity of the silicon alloy particles. XRD pattern of silicon alloy particles shown in Fig. 1(c) indicates that the alloy material consists of Si (PDF#800018), AlFe (PDF#330020), AlNi (PDF#441187) and $TiFeSi_2$ (PDF#752180) phases. The Si peaks were clearly identified and no other impurity peaks could be observed in the XRD pattern. Rietveld method was used to calculate the amount of active silicon that did not participate in the formation of intermetallic alloy.[9] The result revealed that the active Si phase and the inert matrix phases were 55 and 45 wt% in the alloy material, respectively.

The electrochemical performance of the silicon alloy and graphite used to prepare the composite electrodes was

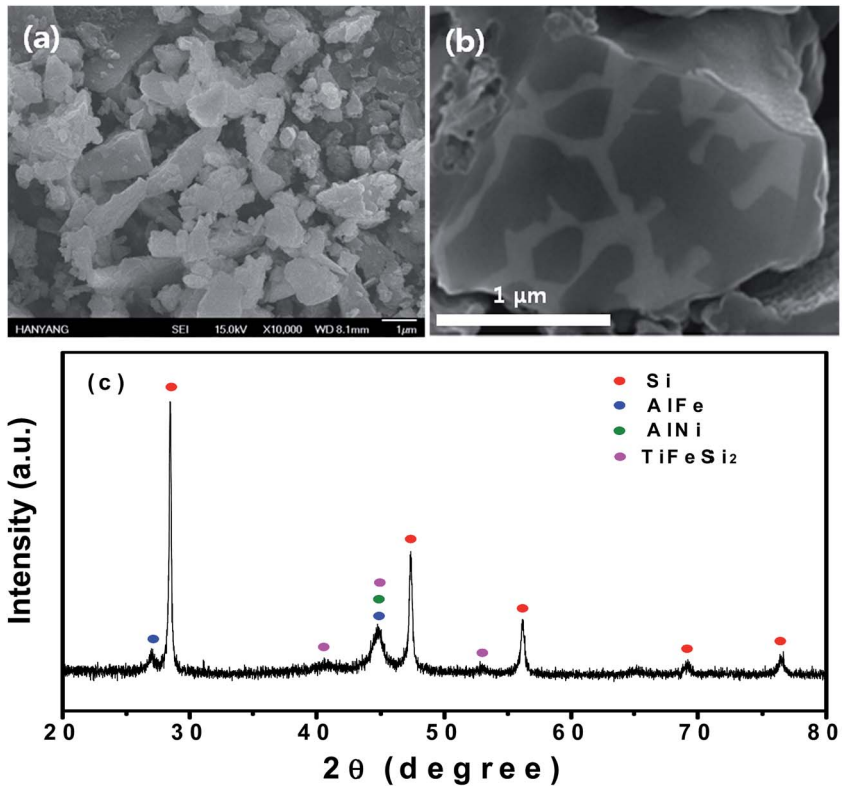

Fig. 1 (a) SEM image and (b) cross-sectional SEM image of silicon alloy particles. (c) XRD pattern of silicon alloy particles.

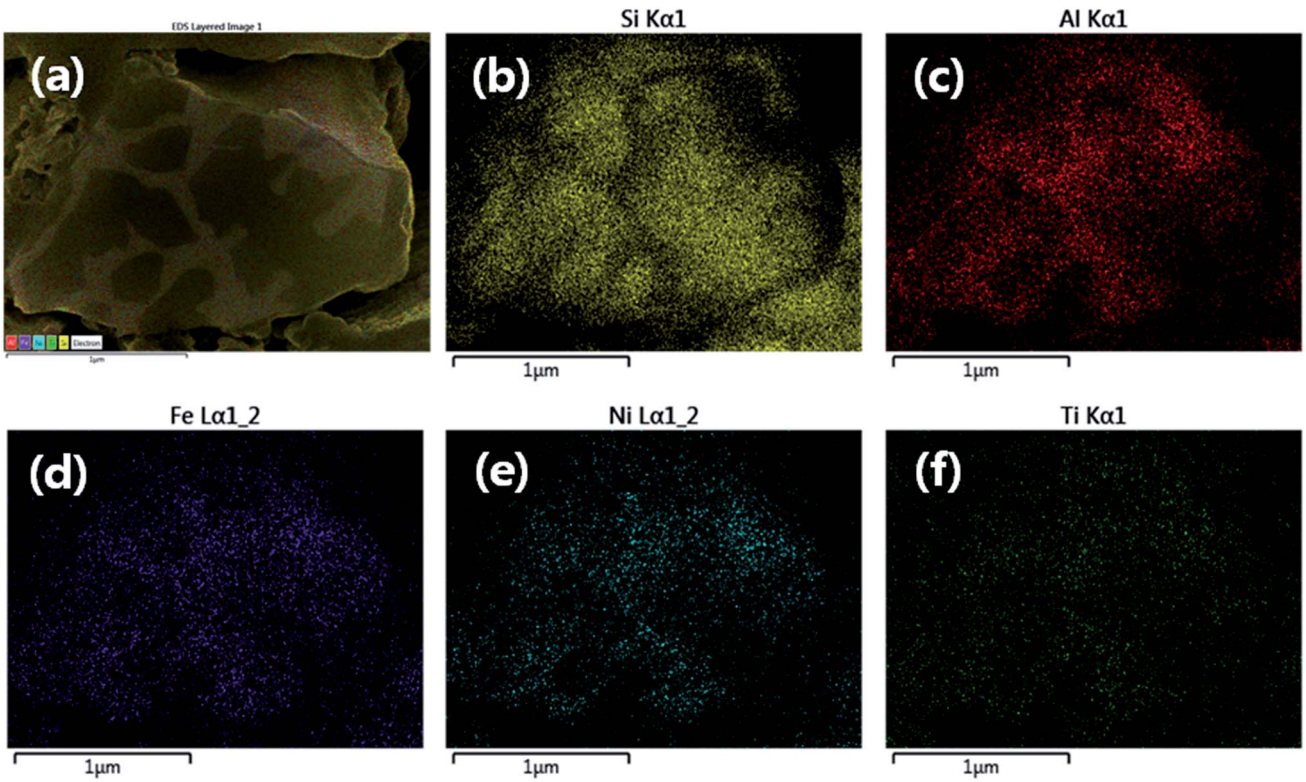

Fig. 2 (a) Cross-sectional SEM image of silicon alloy particles, and EDS mapping images of (b) Si, (c) Al, (d) Fe, (e) Ni, and (f) Ti elements on its cross-section.

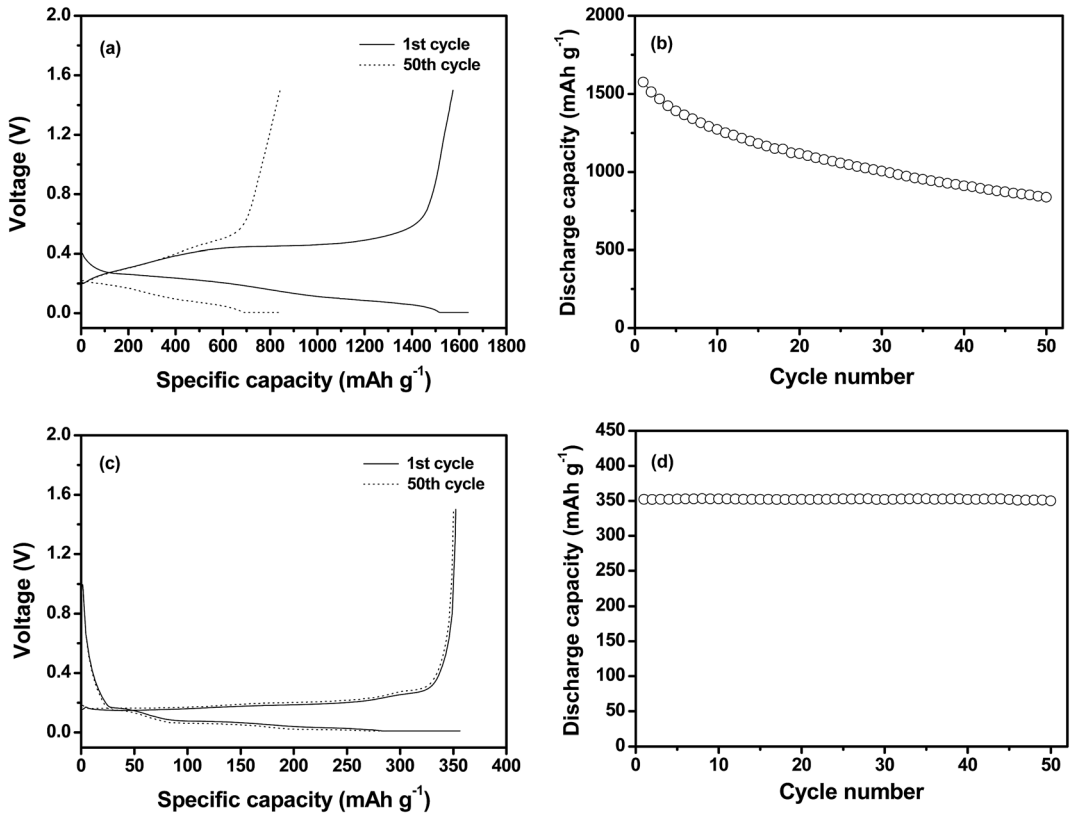

Fig. 3 (a) Charge and discharge curves of the silicon alloy electrode and (b) discharge capacities of the silicon alloy electrode as a function of cycle number. (0.5C constant current (CC) and constant voltage (CV) charge, 0.5C CC discharge, cut-off voltage: 0.005–1.5 V, 25 °C). (c) Charge and discharge curves of the graphite electrode and (d) discharge capacities of the graphite electrode as a function of cycle number. (0.5C CC and CV charge, 0.5C CC discharge, cut-off voltage: 0.01–1.5 V, 25 °C).

evaluated separately. Fig. 3(a) presents the charge and discharge curves of the as-synthesized silicon alloy electrode for the first and 50th cycles, respectively. The Si alloy electrode exhibited typical charge and discharge profiles corresponding to the lithiation of Si and delithiation of Li_xSi, respectively. The initial discharge capacity of the silicon alloy electrode was 1573.9 mA h g^{-1} based on the silicon alloy in the electrode. It corresponds to a volumetric capacity of 5902.1 mA h cm^{-3} based on the volume of silicon alloy material, which is much higher than that (719 mA h cm^{-3}) of commercialized graphite active materials.[30] Although the silicon alloy electrode exhibited a much higher initial capacity than graphite, the electrode exhibited large capacity fading during the repeated cycling, as depicted in Fig. 3(b). The charge and discharge profiles of the graphite electrode shown in Fig. 3(c) exhibited typical curves corresponding to lithium intercalation/de-intercalation processes within graphitic carbon. As shown in Fig. 3(d), the graphite electrode exhibited excellent capacity retention with an initial discharge capacity of 352.4 mA h g^{-1}. In order to prepare anodes with a higher discharge capacity than graphite while maintaining good cycling stability, high-capacity as-synthesized silicon alloy particles were mixed with graphite powder showing good cycling stability for further experiments.

Three-dimensional PVA networks were employed as the binder material in the composite electrodes composed of graphite and silicon alloy, which were synthesized through condensation reactions with PVA and fumaric acid as the cross-linking agent. As schematically demonstrated in Fig. 4(a), the condensation reactions between the hydroxyl groups in PVA and the carboxylic acid groups in fumaric acid formed ester linkages *via* esterification at 150 °C for 1 h, resulting in the formation of three-dimensional cross-linked networks. Prior to cell assembly, FT-IR analysis of the cross-linked PVA films was performed to confirm esterification between PVA and fumaric acid; the resulting FT-IR spectra before and after cross-linking reaction are shown in Fig. 4(b). After cross-linking reaction, the peak corresponding to the C=O group of the carboxylic acid in fumaric acid was shifted from 1671 to 1711 cm^{-1}. This shift demonstrated the formation of an ester linkage *via* esterification between carboxylic acid and hydroxyl groups.[31,32] Additionally, hydroxyl peaks observed between 2500 and 2700 cm^{-1} were no longer present after the condensation reaction. These results implied that the hydroxyl groups in PVA reacted with carboxylic acid groups in fumaric acid *via* esterification to form cross-linked polymer networks.

The cycling performance of the silicon alloy–graphite composite electrodes with cross-linked PVAs was evaluated. The composite electrodes were initially subjected to two preconditioning cycles in the voltage range of 0.01 to 1.5 V at 0.2C rate. The current rate (0.2C) in the preconditioning cycle was

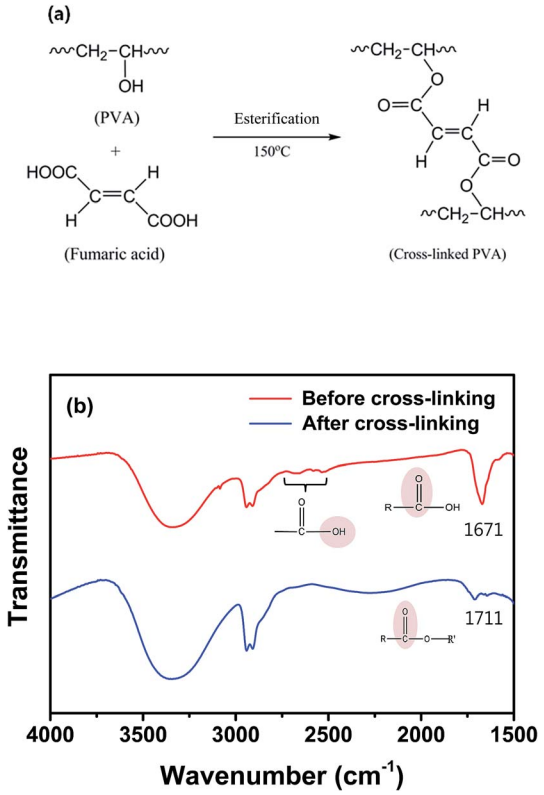

Fig. 4 (a) Schematic representation of the cross-linking of poly(vinyl alcohol) (PVA) binders through esterification between PVA and fumaric acid, and (b) FT-IR spectra of the PVA film before and after the cross-linking reaction.

lower than the current rate (0.5C) for the cycling test in order to effectively form a solid electrolyte interphase (SEI) layer on the electrode surface during the initial cycles. Fig. 5(a) reveals the first preconditioning charge and discharge curves of the composite electrodes prepared with different amounts of cross-linking agent. All electrodes exhibited nearly identical profiles with relatively high initial coulombic efficiencies (~89.1%). The irreversible capacity observed in the first cycle was attributed to SEI layer formation due to reductive decomposition of the liquid electrolyte.[33,34] The initial discharge capacity of the composite electrodes was decreased from 472.1 to 457.7 mA h g^{-1} with increasing content of cross-linking agent. The cross-linking reaction caused an increase in the resistance for Li^+ ion transport due to the formation of three-dimensional polymer networks within the composite electrode, resulting in a decreased discharge capacity with increasing cross-linking density. The initial discharge capacities of all the composite electrodes were much higher than that of the graphite electrode (352.4 mA h g^{-1}). After two preconditioning cycles, the cells were cycled in the voltage range of 0.01 to 1.5 V at a rate of 0.5C. Fig. 5(b) presents the charge and discharge curves for the composite electrode employing the PVA-5.0 binder. The electrode initially delivered a discharge capacity of 454.1 mA h g^{-1} with a coulombic efficiency of 98.6%. Higher coulombic efficiency after two preconditioning cycles indicated that reductive decomposition of the electrolyte solution was suppressed by the

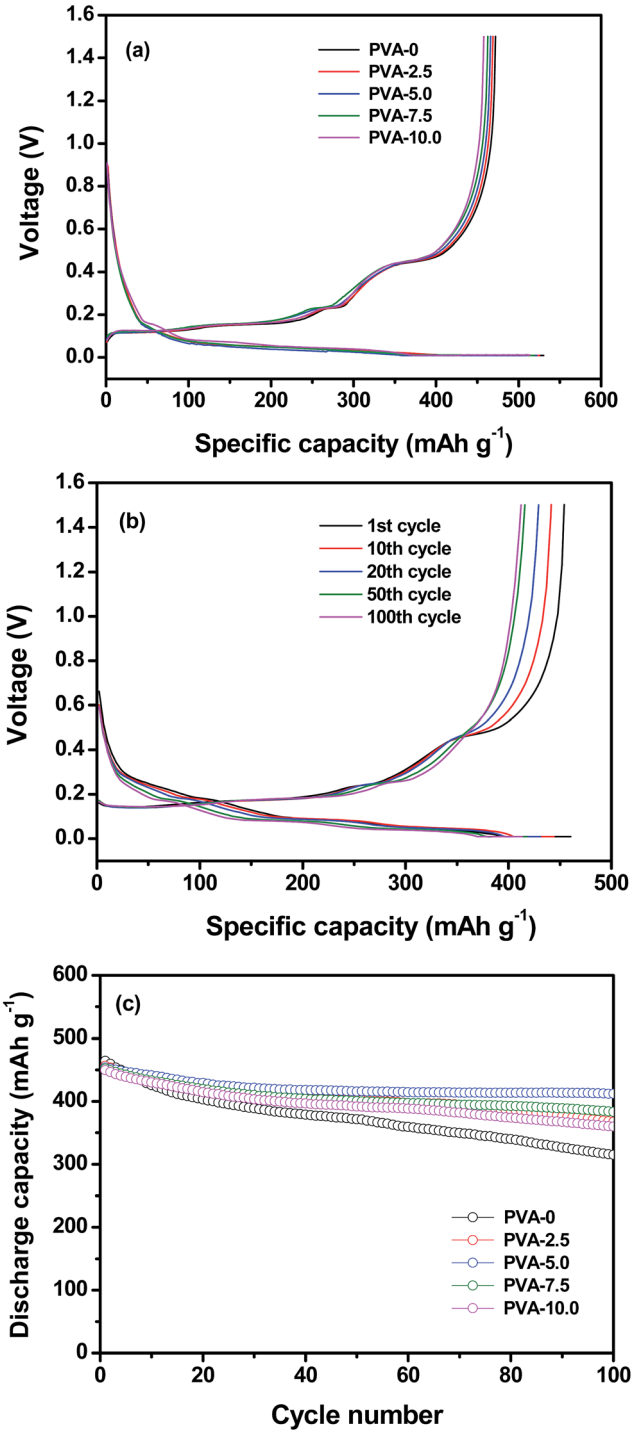

Fig. 5 (a) Preconditioning charge and discharge curves of the composite electrodes with cross-linked PVA binders (0.2C rate, cut-off voltage: 0.01–1.5 V), (b) charge and discharge curves of the composite electrode with cross-linked PVA (PVA-5.0) (0.5C CC and CV charge, 0.5C CC discharge, cut-off voltage: 0.01–1.5 V), (c) discharge capacities of the composite electrodes employing PVAs with different degrees of cross-linking. (0.5C CC and CV charge, 0.5C CC discharge, cut-off voltage: 0.01–1.5 V).

SEI layer formed during the preconditioning cycles. The coulombic efficiency steadily increased with cycling and was maintained at >99.6% throughout the cycling after

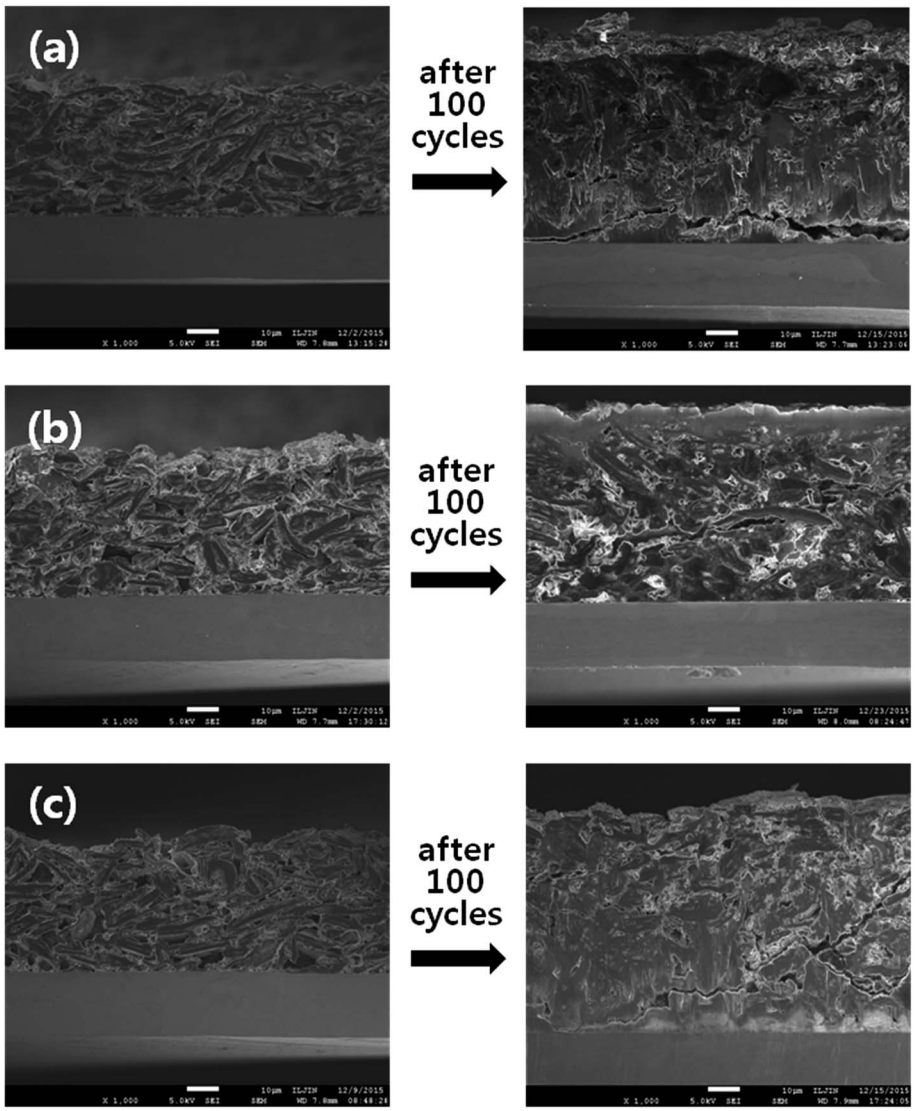

Fig. 6 Cross-sectional SEM images of different composite electrodes before and after 100 cycles: (a) PVA-0 electrode, (b) PVA-5.0 electrode, and (c) PVA-10.0 electrode.

stabilization. Fig. 5(c) presents the discharge capacities of the composite electrodes employing cross-linked PVAs with different amounts of cross-linking agent for 100 cycles at a rate of 0.5C. As shown in figure, the degree of PVA cross-linking affected the cycling stability of the electrodes. The composite electrode without cross-linking exhibited large capacity fading during cycling. In contrast, the composite electrode employing cross-linked PVAs exhibited more stable cycling characteristics and relatively higher discharge capacities during cycling. The formation of three-dimensional cross-linked PVA networks within the electrode could reduce cracks or pulverization of the silicon alloy active material, as well as maintain good electrical contacts between the silicon alloy particles, graphite powder and conducting carbon, leading to good capacity retention. However, excessive cross-linking of PVA beyond 5.0 wt% fumaric acid in the electrode adversely affected the cycling stability. These results can be attributed to an increase in electrode brittleness due to excessive cross-linking, which could not effectively buffer the volumetric changes of the electrodes during cycling. Based on these results, the optimum content of cross-linking agent to achieve the best cycling stability was about 5.0 wt%.

In order to investigate the effect of cross-linking on the interfacial contacts of the composite electrodes, the cross-sectional FE-SEM images of composite electrodes were examined before and after 100 cycles. As shown in Fig. 6(a), the electrode detachment from the current collector was observed in the electrode without cross-linking, arising from mechanical stress due to large volumetric changes of the silicon alloy particles during charging and discharging. As a result, a loss of electrical conduction paths in the electrode might have been a primary cause of the large decrease in capacity. On the other hand, electrical contacts between the active materials, conducting carbon and copper foil were well maintained in the

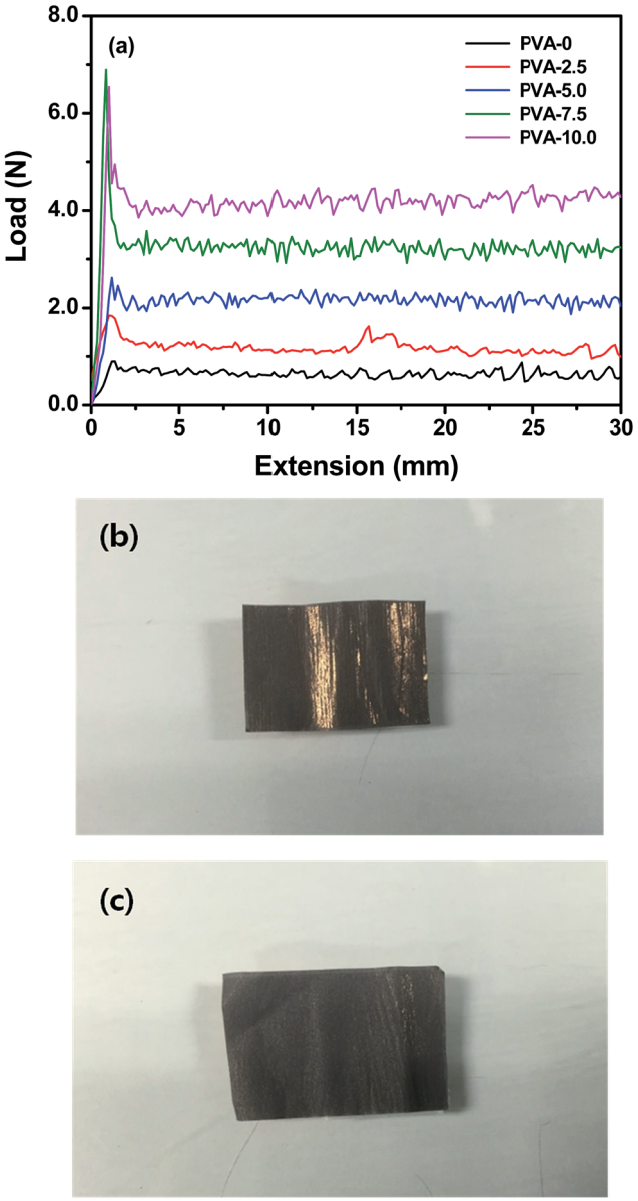

Fig. 7 (a) Adhesive forces measured between electrode and current collector in the composite electrodes employing PVAs with different degrees of cross-linking. Photo images of (b) PVA-0 and (c) PVA-5.0 electrodes after peel test.

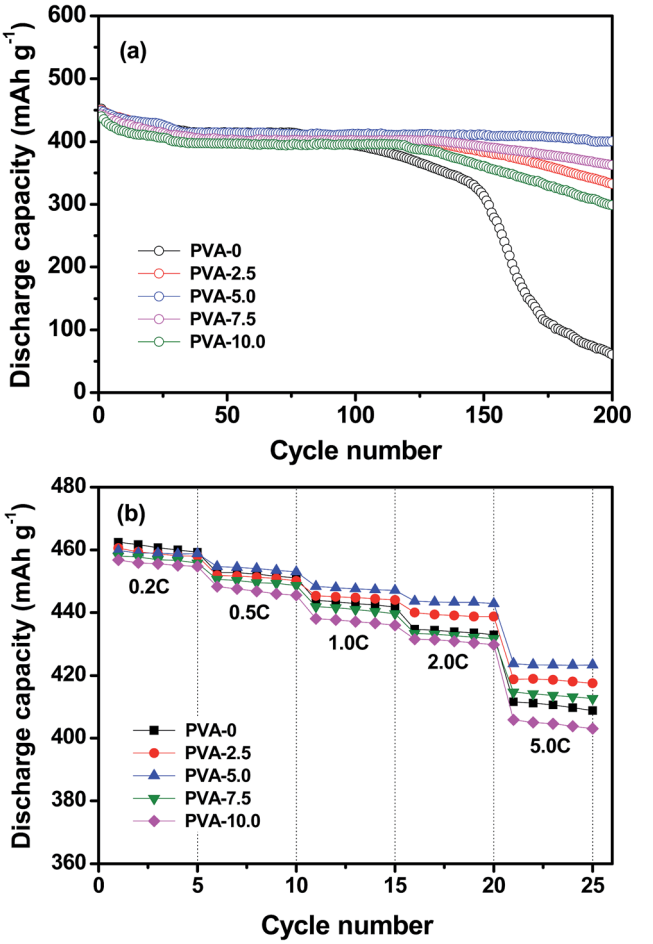

Fig. 8 (a) Discharge capacities of the composite electrodes employing PVAs with different degrees of cross-linking. (1.0C CC and CV charge, 1.0C CC discharge, cut-off voltage: 0.01–1.5 V). (b) Discharge capacities of the composite electrodes with the C rate increasing from 0.2 to 5.0C every five cycles.

PVA-5.0 electrode, as seen in Fig. 6(b). These results suggest that the good cycling stability of the composite electrode (PVA-5.0) was closely related to the strong binding property of the cross-linked PVA networks, providing a robust electrode structure during cycling. However, large cracks were observed in the PVA-10.0 electrode, although the composite electrode was well attached to the current collector (Fig. 6(c)). As the degree of cross-linking excessively increased, the electrode became brittle and hard, which could not endure the mechanical stress caused by volumetric changes and cracks generated within the electrode, as reported earlier.[32] These results suggest that a proper amount of cross-linking agent should be used to maintain interfacial contacts between the active materials, conducting carbon and copper foil, as well as to effectively buffer volumetric changes of the electrode.

To evaluate the adhesive strength of the composite electrodes, a peel test was performed for the composite electrodes employing PVAs with different degrees of cross-linking; the results are shown in Fig. 7(a). As seen in the figure, composite electrodes with cross-linked PVA binders exhibited stronger adhesive forces toward copper foil than did the electrodes that were not cross-linked. The adhesive strength gradually increased with increase in the degree of cross-linking. Fig. 7(b) and (c) show the surface of the electrodes after the peel test. Clearly, the PVA-0 electrode without cross-linking completely detached from the current collector after the peel test. In contrast, the electrode with cross-linked PVA (PVA-5.0) was well attached to the current collector due to its strong binding ability. Based on these results, we concluded that the cross-linking of PVAs enhanced the adhesion between silicon alloy particles, graphite powder, conducting carbon and current collector, enabling the electrode to maintain good capacity retention during cycling.

To further demonstrate the beneficial effect of cross-linking of PVA on the cycling stability, the cycling test of the composite electrodes was further carried out at 1.0C rate. Fig. 8(a) shows the discharge capacities of the composite electrodes employing PVAs with different degrees of cross-linking at 1.0C rate. It is clearly seen that the composite electrodes employing cross-linked PVAs exhibited better capacity retention than the composite electrode without cross-linking. Even at a high current rate of 1.0C, the PVA-5.0 electrode initially delivered high discharge capacity of 448.9 mA h g^{-1} and exhibited stable cycling characteristics. In contrast, the composite electrode without cross-linking (PVA-0) showed a significant capacity fading after 100 cycles. Fig. 8(b) compares the discharge capacities of the composite electrodes employing cross-linked PVAs with different amounts of cross-linking agent, with the C-rate increasing from 0.2 to 5.0C after every five cycles. As expected, the discharge capacities decreased with increasing the C rate due to polarization. The effect of the degree of cross-linking on the rate performance of the composite electrodes was noticeable as the current rate was increased from 0.2C to 5.0C. Both the rate capability and cycling stability were improved by increasing the content of the cross-linking agent up to 5.0 wt%. As discussed earlier, the three-dimensional polymer network served as a strong adhesive to bind the active materials and conductive carbon together; strong adhesive forces in the electrode also prevented the active materials from detaching from the electrode at high cycling rates, resulting in a high rate capability. However, the high rate performance decreased when the content of cross-linking agent was further increased to 10.0 wt%. Excessive cross-linking might have blocked the penetration of liquid electrolyte into the porous electrodes, resulting in an increase of resistance for ion migration in the electrodes.[35,36] These results imply that proper control of the cross-linking density within the electrode is very important for achieving both good capacity retention and high rate capability.

Conclusions

The composite electrodes composed of high-capacity silicon alloy (silicon nanoparticles embedded in Al–Fe–Ti–Ni matrix phases) and graphite with good cycling stability were prepared, and their electrochemical characteristics were investigated. PVAs with different degrees of cross-linking were used as the polymer binder in the composite anodes. Cross-linking of PVA with a proper amount of fumaric acid improved the mechanical integrity of the electrodes by maintaining good interfacial contact between the active materials, conducting carbon and current collector, resulting in an improvement in cycling performance such as discharge capacity, capacity retention and rate capability. These silicon alloy-based composite electrodes exhibiting higher capacity than commercially available graphite showed good potential for use as the anode in high-energy density lithium-ion batteries.

Acknowledgements

This work was supported by the green industry leading secondary battery technology development program of KEIT (10046341, Development of a high-capacity, low-cost, silicon-based anode material for lithium secondary batteries) and by the Basic Science Research Program through the National Research Foundation of Korea (NRF), funded by the Ministry of Science, ICT, and Future Planning (2014R1A2A2A01002154).

References

1 M. Armand and J. M. Tarascon, *Nature*, 2008, **451**, 652–657.
2 B. Scrosati, J. Hassoun and Y. K. Sun, *Energy Environ. Sci.*, 2011, **4**, 3287–3295.
3 V. Etacheri, R. Marom, R. Elazari, G. Salitra and D. Aurbach, *Energy Environ. Sci.*, 2011, **4**, 3243–3262.
4 B. Liang, Y. Liu and Y. Xu, *J. Power Sources*, 2014, **267**, 469–490.
5 C. K. Chan, H. Peng, G. Liu, K. McIlwrath, X. F. Zhang, R. A. Huggins and Y. Cui, *Nat. Nanotechnol.*, 2008, **3**, 31–35.
6 H. Wu, G. Chan, J. W. Choi, I. Ryu, Y. Yao, M. T. McDowell, S. W. Lee, A. Jackson, Y. Yang, L. B. Hu and Y. Cui, *Nat. Nanotechnol.*, 2012, **7**, 309–314.
7 H. Kim, M. Seo, M. H. Park and J. Cho, *Angew. Chem., Int. Ed.*, 2010, **49**, 2146–2149.
8 J. Yu, N. Du, H. Zhang and D. Yang, *RSC Adv.*, 2013, **3**, 7713–7717.
9 S.-B. Son, S. C. Kim, C. S. Kang, T. A. Yersak, Y.-C. Kim, C.-G. Lee, S.-H. Moon, J. S. Cho, J.-T. Moon, K. H. Oh and S.-H. Lee, *Adv. Energy Mater.*, 2012, **2**, 1226–1231.
10 B. C. Yu, H. Y. Kim, C. H. Park, S. K. Kim, J. W. Sung and H. J. Sohn, *Electrochim. Acta*, 2014, **130**, 583–586.
11 M. T. McDowell, S. W. Lee, C. Wang and Y. Cui, *Nano Energy*, 2012, **1**, 401–410.
12 N. Dimov, S. Kugino and A. Yoshio, *J. Power Sources*, 2004, **136**, 108–114.
13 G. Zeb, P. Gaskell, Y. N. Kim, G. Jalani, X. Xiao, T. Szkopek and M. Cerruti, *RSC Adv.*, 2016, **6**, 45519–45524.
14 K. E. Aifantis and S. A. Hackney, *J. Power Sources*, 2011, **196**, 2122–2127.
15 C.-H. Yim, F. M. Courtel and Y. Abu-Lebdeh, *J. Mater. Chem. A*, 2013, **1**, 8234–8243.
16 T. Yim, S. J. Choi, J. H. Park, W. Cho, Y. N. Jo, T. H. Kim and Y. J. Kim, *Phys. Chem. Chem. Phys.*, 2015, **17**, 2388–2393.
17 A. G. Kannan, S. H. Kim, H. S. Yang and D.-W. Kim, *RSC Adv.*, 2016, **6**, 25159–25166.
18 J. Li, R. B. Lewis and J. R. Dahn, *Electrochem. Solid-State Lett.*, 2007, **10**, A17–A20.
19 N. S. Choi, K. H. Yew, W. U. Choi and S. S. Kim, *J. Power Sources*, 2008, **177**, 590–594.
20 I. Kovalenko, B. Zdyrko, A. Magasinski, B. Hertzberg, Z. Milicev, R. Burtovyy, I. Luzinov and G. Yushin, *Science*, 2011, **334**, 75–79.
21 C. Kim, J. Y. Jang, N.-S. Choi and S. Park, *RSC Adv.*, 2014, **4**, 3070–3074.
22 H. S. Yang, S.-H. Kim, A. G. Kannan, S. K. Kim, C. Park and D.-W. Kim, *Langmuir*, 2016, **32**, 3300–3307.
23 M. Ling, Y. N. Xu, H. Zhao, X. X. Gu, J. X. Qiu, S. Li, M. Y. Wu, X. Y. Song, C. Yan, G. Liu and S. Q. Zhang, *Nano Energy*, 2015, **12**, 178–185.

24 Y. K. Jeong, T. W. Kwon, I. Lee, T. S. Kim, A. Coskun and J. W. Choi, *Energy Environ. Sci.*, 2015, **8**, 1224–1230.
25 Y. Park, S. Lee, S.-H. Kim, B. Y. Jang, J. S. Kim, S. M. Oh, J.-Y. Kim, N.-S. Choi, K. T. Lee and B.-S. Kim, *RSC Adv.*, 2013, **3**, 12625–12630.
26 M. Kim, J.-W. Kim, M.-S. Sung, Y. Hwa, S. H. Kim and H.-J. Sohn, *J. Electroanal. Chem.*, 2012, **687**, 84–88.
27 M.-S. Park, Y.-J. Lee, S. Rajendran, M.-S. Song, H.-S. Kim and J.-Y. Lee, *Electrochim. Acta*, 2005, **50**, 5561–5567.
28 S. J. Park, H. Zhao, G. Ai, C. Wang, X. Y. Song, N. Yuca, V. S. Battaglia, W. L. Yang and G. Liu, *J. Am. Chem. Soc.*, 2015, **137**, 2565–2571.
29 C. Hwang, Y. G. Cho, N. R. Kang, Y. Ko, U. Lee, D. Ahn, J. Y. Kim, Y. J. Kim and H. K. Song, *J. Power Sources*, 2015, **298**, 8–13.
30 M. N. Obrovac and V. L. Chevrier, *Chem. Rev.*, 2014, **114**, 11444–11502.
31 B. Koo, H. Kim, Y. Cho, K. T. Lee, N.-S. Choi and J. Cho, *Angew. Chem., Int. Ed.*, 2012, **51**, 8762–8767.
32 J. Song, M. Zhou, R. Yi, T. Xu, M. L. Gordin, D. Tang, Z. Yu, M. Regula and D. Wang, *Adv. Funct. Mater.*, 2014, **24**, 5904–5910.
33 R. Fong, U. Vonsacken and J. R. Dahn, *J. Electrochem. Soc.*, 1990, **137**, 2009–2013.
34 J. M. Tarascon and D. Guyomard, *J. Electrochem. Soc.*, 1991, **138**, 2864–2868.
35 M. Wu, X. Xiao, N. Vukmirovic, S. Xun, P. K. Das, X. Song, P. Olalde-Velasco, D. Wang, A. Z. Weber, L.-W. Wang, V. S. Battaglia, W. Yang and G. Liu, *J. Am. Chem. Soc.*, 2013, **135**, 12048–12056.
36 C. Chen, S. H. Lee, M. Cho, J. Kim and Y. Lee, *ACS Appl. Mater. Interfaces*, 2016, **8**, 2658–2665.